In-situ Ultrasound Acoustic Measurement of the Lithium-ion Battery Electrode Drying Process

Ye Shui Zhang[1,2], Anand Narayanan Pallipurath Radhakrishnan [1], James B. Robinson[1,2], Rhodri E. Owen[1,2], Thomas G. Tranter[1,2], Emma Kendrick[2,3], Paul R. Shearing[*1,2], Dan J.L. Brett[*1,2]

[1.] Electrochemical Innovation Lab, Department of Chemical Engineering, University College London, London, UK WC1E 7JE

[2.] The Faraday Institution, Quad One, Harwell Science and Innovation Campus, Didcot, UK OX11 0RA

[3.] School of Metallurgy and Materials, University of Birmingham, Birmingham, UK B15 2TT

(Corresponding authors: Dan Brett d.brett@ucl.ac.uk & Paul Shearing p.shearing@ucl.ac.uk)

Keywords: LIBs, electrode drying process, ultrasound acoustic measurement, drying mechanism, drying dynamics

Supporting Information. Supporting figures and comparison between thermogravimetric analysis and ultrasound acoustic measurement to investigate the Li-ion electrode drying process has been addressed.

Acknowledgement

This work was supported by the Faraday Institution [grant number FIRG015] and the EPSRC (EP/R020973/1).

Abstract

The electrode drying process is a crucial step in the manufacture of lithium-ion batteries and can significantly affect the performance of an electrode once stacked in a cell. High drying rates may induce binder migration which is largely governed by the temperature. Additionally, elevated drying rates will result in a heterogeneous distribution of soluble and dispersed binder throughout the electrode, potentially accumulating at the surface. The optimized drying rate during the electrode manufacturing process will promote balanced homogeneous binder distribution throughout the electrode film; however, there is a need to develop more informative *in-situ* metrologies to better understand the dynamics of the drying process. Here, ultrasound acoustic based techniques have been developed as an *in-situ* tool to study the electrode drying process using NMC622-based cathodes and graphite-based anodes. The drying dynamic evolution for cathodes dried at 40 and 60 °C, and anodes dried at 60 °C were

investigated, with the attenuation of the reflective acoustic signals used to indicate the evolution physical properties of the electrode coating film. The drying-induced acoustic signal shifts were discussed critically and correlated to the reported three-stage drying mechanism, which offering a new mode to investigate the dynamic drying process. Ultrasound acoustic based measurements have been successfully shown to be a novel *in-situ* metrology to acquire dynamic drying profiles of lithium-ion battery electrodes. The findings would potentially fulfil the research gaps between acquiring dynamic data continuously for drying mechanism study and existing research metrology, as the most of the published drying mechanism researches were based on a simulated drying process. It shows the great potential to be further developed and understand the drying process to achieve a more controllable electrode manufacturing process.

1 Introduction

Lithium-ion batteries (LIBs) are ubiquitous within portable applications such as mobile phones, laptops and increasingly used in e-mobility due to their relatively high energy and power density [1]. The manufacturing process of these LIBs has largely remained the same since their initial commercialisation by Sony in the 1990s [2]. In general, the electrode manufacturing process consists of mixing, coating, drying, calendaring and post-drying. The common composites for typical LIB electrodes consist of active materials (AM) with particle sizes of ~10-20 µm, conductive additives with particle sizes of ~100 nm, and binder (polymeric or water-soluble)[3]. Common cathode AMs include $LiNixCoyMnzO_2$ (NMC), $LiNixCoyAlzO_2$ (NCA), $LiMn_2O_4$ and $LiFePO_4$ (LFP), etc. For the anode, graphite is typically adopted, sometimes with added silicon, and in some cells $Li_4Ti_5O_{12}$ (LTO). The active components of the negative and positive electrodes are mixed separately into a slurry containing a conductive additive, such as carbon black (CB) and a polymeric binder (e.g., polyvinylidene fluoride, PVDF) in a solvent such as N-methyl-2-pyrrolidone (NMP). The carbon binder domain (CBD) promotes mechanical integrity and electron transport, whereas the pores left by evaporated solvent are filled with electrolyte, promoting lithium-ion transportation, both directly affecting the performance of the battery by varying mass transport properties [4]. The slurry is then tape-cast onto a current collector (CC) – Cu foil for the negative electrode and Al foil for the positive electrode. The resulting coating is then dried to produce a cohesive film which adheres to the CC. The drying temperature is in a range between room temperature [5] to 120 °C [3] depends on the composition and types of the solvent. The dried electrode is then calendared to reduce the electrode thickness, increasing 3D connectivity, electron conductivity and maximising the volumetric energy density [3].

A homogeneous, defect-free coating is required to achieve consistency within LIB electrodes, with target weights realised throughout the coating film. This enables homogeneous current densities and lithium transport between the electrodes, to improve cell performance and reduce the failure. Although the wet processing of electrodes has developed into a well-established technique in the electrode manufacturing industry [6-10], there are still unresolved issues with the process, such as coating inconsistency and microstructure defects which can occur during the drying process (DP) [5, 11]. Researches have shown that the microstructure and morphology of the LIB electrodes are strongly dependent on the manufacturing process, especially upon the drying protocol [5, 12-14]. Hawley and Li [5] have recently reviewed LIB electrode manufacturing processes and noted that the electrochemical performance of an electrode is dominantly affected by the drying parameters. The rate of drying is governed by specific drying mechanisms and seeking an optimal drying rate necessitates an in-depth understanding of these mechanisms. Solvent elimination plays a key role in next-generation smart electrode manufacturing [5]. To better control the properties of an electrode, it is imperative to improve our understanding of the drying dynamics [15], and thus provide the means for manufacturing-tailored electrode architectures that can unlock the further potential of LIBs [5]. Further, an improved understanding of the mechanisms behind the DP may facilitate a reduction in both the time and energy expenditure required to produce electrodes. Yuan *et al*. have estimated that the drying process accounts for over 47% and 60% of the energy consumed on a per cell basis and the time taken to produce electrodes, respectively [16-17].

Various aspects of the electrode DP have been the subject of recent studies [12-13, 15, 18-26]. Effective control of the electrode DP requires a series of advanced analytical techniques that needs to facilitate both *in-situ* and/or *ex-situ* characterization of the sample of interest [9, 27-29]. The influence of drying parameters/variables on the properties of the finished electrode is extremely complex. Parameters such as the drying rate, binder types and formulation, affect the final properties of the electrodes. The drying rate is controlled by the temperature, pressure, IR (infrared) radiation intensity and airflow, depending on the drying method used. The types of binder directly correlate with the drying time, with slurries formed using aqueous binders taking a shorter time to dry, compared to slurries produced with organic-based binders. The choice of drying conditions also has a strong influence on the typical defects observed in electrodes. These include the binder induced migration of the electrode coating, delamination of the coating layer from the CC, electrode film shrinkage and the component segregation of the coating. Correspondingly, these defects will affect the microstructure of the formed electrode, adhesion strength between the electrode coating and the CC, cell capacity, resistivity and cycling performance.

Previous investigations have primarily focussed on *ex-situ* characterisation of the influence of drying conditions on the electrodes properties; this includes surface morphology, microstructure, elemental distribution, particle microstructure, pore size distribution, and thickness [5, 18, 22-23, 30-38]; with *in-situ* characterisation methods rarely applied during the DP. Although some *in-situ* techniques have been applied to study the microstructural evolution [37], drying rate [18-20, 25, 37, 39-40] , binder and particles distribution [18-20, 25] or stress development during drying [40]. Despite this, reports of the dynamic conditions observed during the DP are sparse due to the limited capability of these techniques.

Ultrasound acoustic-based techniques are being increasingly used to monitor batteries during operation (*in-operando*). Hsieh *et al.* [41] demonstrated the feasibility of this technique through ultrasound acoustic time-of-flight (ToF) measurements to study the physical dynamics of batteries under different states of charge. Observing a change in the acoustic signal's attenuation, the authors reported that the distribution of density and bulk moduli of both electrodes within a cell had changed with varying states of charge. Davies *et al.* [42] also attributed the shifts of the transmitted ultrasonic signals to be caused by the change of electrode density and bulk modulus. Robinson *et al.* [43] spatially mapped the lithiation and delithiation of electrodes in a commercial mobile phone battery by using ultrasound acoustic measurements. The lithiation and delithiation of the electrodes resulted in a density variation that could be identified by analysing the signal changes during the charging process. Recently, Deng *et al.* [44] developed an ultrasonic imaging technique to study the internal changes of a pouch cell by measuring its local ultrasonic transmittance non-destructively. The work demonstrated the potential to observe the wetting process with high very sensitivity to probe the failure mechanism. These experimental results have highlighted the effectiveness of acoustic-based techniques as an *operando* method to study the physical changes of a battery during cycling.

The application of ultrasound acoustic-based techniques is based on the attenuation of the ultrasound waves. The intensity diminishes with distance when sound travels through a medium/material. Also, the properties of the natural materials will further weakens the sound wave which results from scattering and absorption [45]. Ultrasonic attenuation is the decay rate of the wave as it propagates through material. Attenuation often serves as a measurement tool that leads to the formation of theories to explain physical or chemical phenomenon that decreases the ultrasonic intensity. The amplitude change of a wave can be expressed as Equation 1 [45]:

$$P(x,t) = P_0 e^{-\alpha x} cos(\omega t - kx) \qquad \textit{Equation 1}$$

Where $\mathbf{P_0}$ is the un-attenuated amplitude of the propagating wave; **P** is the reduced amplitude after the wave has travelled a distance **x** from initial location; **e** is the Napier's constant is ~ 2.71828; **α** is the frequency-dependent amplitude attenuation coefficient of the wave traveling in the **x**-direction; $\boldsymbol{\omega}$ is radian frequency; $\boldsymbol{k}$ is the wave number [45]. Attenuation is generally proportional to the square of sound frequency [45]. Also, the actual value of the attenuation coefficient for a given material is highly dependent on the way in which the material was manufactured. Attenuation can be determined by evaluating the multiple backwall reflections. The number of decibels between two adjacent signals is measured and this value is divided by the time interval between them. This calculation produces an attenuation coefficient in decibels per unit time $\mathbf{U_t}$ which can be converted to nepers/length by the following equation [45],

$$a = \frac{0.1151}{v} U_t \qquad \textit{Equation 2}$$

Where **v** is the velocity of sound in meters per second and $\mathbf{U_t}$ is in decibels per second [45]. As an LIB electrode DP is mostly governed by physical phenomena, such as solvent phase-change, density and porosity variations in the electrode coating etc., the ultrasound acoustic technique represents a flexible, scalable and simple *in-situ* method to investigate this dynamic process.

In this work, an ultrasound acoustic technique has been developed as an *in-situ* tool to analyse the LIB electrode DP. The attenuation of the reflective acoustic signals directly correlate with the evolving physical properties of the electrode coating film, as drying progressed. Upon completion of the DP, the electrochemical properties of the electrodes were tested in coin cells to elucidate the temperature effects on the electrochemical performance. A critical discussion about the drying-induced acoustic signal shifts has been discussed, offering new insights into the dynamics of drying.

2 Materials and experimental set-up

2.1 Materials

The raw materials and the formulations of the cathodes and anodes prepared for this study are shown in Table 1. The formulations for both anode and cathode in this work are generic formulations that are extensively employed as reported by Kendrick [3]. To form the cathode slurry, $LiNi_{0.6}Mn_{0.2}Co_{0.2}O_2$ (NMC622, BASF), polyvinylidene fluoride (PVDF, Solvay) and C_{65} (Imerys) powders were pre-dried at 120 °C in a vacuum oven overnight to ensure that the mixture had no moisture. 13 ml of N-methyl-2-pyrrolidone (NMP, Sigma Aldrich) mixed with 0.4 g of PVDF was then weighed to form a binder solution. A THINKY mixer (ARE-20, Intertronics) was used to mix the cathode binder solution (PVDF and NMP) at 2000 rpm for 15 min until the solution became homogenous. Then, 19.3 g of NMC622 and 0.4 g of C_{65} was

added slowly to the binder solution to form a slurry with a solid content ~60 wt.%. The slurry was then mixed again at 2000 rpm for 2 periods of 15 min, with 5 min in between to cool down the slurry. The homogenous slurry was degassed in the THINKY mixer at a speed of 2000 rpm for 2 min. To prepare the anode slurry, carboxymethyl cellulose (CMC) was firstly pre-dissolved in water to make a 1.5% solution. The weighed Artificial Graphite, C_{45}, the 1.5% CMC solution, and styrene-butadiene rubber (SBR) were added into a THINKY pot to form a slurry with 44 wt.% solid content. The mixing procedure was same as that used for the cathode slurry preparation.

Table 1 Formulation and raw material details for cathodes and anodes.

Material	Model	Formulation	Supplier
Cathode active material	NMC 622	96.0 wt.%	BASF
Cathode binder	PVDF 5130	2.0 wt.%	Solvay
Conductive additive	C_{65}	2.0 wt.%	Imerys
Anode active material	S360-E3 Artificial Graphite	95.25 wt.%	BTR
Anode binder 1	CMC BVH8	1.5 wt.%	Ashland
Anode binder 2	SBR BM451-B	2.25 wt.%	Zeon
Conductive additive	C_{45}	1.0 wt.%	Imerys

The cathode slurry was then coated on a piece of aluminium foil with thickness ~16 µm (PI-KEM) using a doctor blade thin-film applicator (calibrated with a metal shim), resulting in a wet electrode of ~280 µm thickness. The anode slurry was coated on a copper foil with thickness ~9 µm (Phi-Chem) using a similar procedure, resulting in ~300 µm thick slurry coating. The coatings were dried for varying lengths of time in a pre-heated oven (Binder) at 40 and 60 °C.

2.2 Experimental set-up

2.2.1 Ultrasound acoustic measurement

All ultrasound acoustic measurements were performed by an Olympus Epoch 650 ultrasonic flaw detector (Olympus Corp., Japan) using a 9 mm diameter piezoelectric transducer operated at a frequency of 5 MHz (M110-RM , Olympus Corp., Japan). The experimental set-up is shown in supplementary information (SI) Figure 1 (a). which was aiming to simulate the drying environment in the 3 zone dryer as a semi-industrial drying process from Warwick Manufacturing Group (WMG), The University of Warwick [46] Acoustic measurements were performed by placing the transducer underneath the CC (the electrode slurry coating on the upper side of the CC) with a thin layer of aqueous ultrasonic gel (VWR International, USA) between the transducer and the CC. Measurements were obtained using a range of acoustic

gain between 40-70 dB with no delay imposed on the measurements. The range of gain was determined manually to obtain the highest possible signal response (close to 100% acoustic response) for the initial interface layers without saturating the receiver. The resolution of the output of the acoustic reading was limited to 495 discrete measurements to describe the reflection signals. As a result, the duration of the measurements was limited to 10 µs range which provided a resolution of 2.5 ns in the acquired signals. This provided information on the first overlapping peaks associated with the CC and electrode coating interfaces with sufficient signal responses to enable confident analysis. The Epoch 650 was controlled using a bespoke algorithm developed using LabVIEW 2019 (National Instruments, UK) and a script written using the Python programming language. This allowed a continuous monitoring of the process with a user-controlled discrete sampling and the resulting measurements saved as a series of CSV files. The acoustic signals were acquired over the entire drying process, until no significant changes to the signals were observed. To confirm that the electrodes were dried, the residual moisture/solvent content after cathode drying at 60 °C was measured using a thermal gravimetric analysis (TGA) (Perkin Elmer Pyris 1 TGA). Approximately 4-8 mg of dried cathode was placed in a platinum sample crucible and heated to 80 ^{o}C with 20 mL min^{-1} argon flow rate. The solvent residue was ~0.4 wt.%, as shown in Figure S1 (b). Each experimental condition was repeated at least four times to ensure reproducibility.

2.2.2 Electrochemical performance Test

After acoustic measurements, the electrodes were cut into 15 mm discs for making coin cells. A Celgard separator was cut into 19 mm discs to avoid short circuit. All the coin cell components, namely the cut electrodes, separators, and other coin cell parts (spacer thickness 1 mm) were dried in a vacuum oven at 80 °C overnight to remove any moisture before assembly. After the assembly of the coin cell, a formation step composed of two C/20 CC-CV charge (C/50 cut-off) and C/10 CC discharge cycles were conducted within the voltage window 2.5 to 4.2 V for cathode half cells and 0 to 1.5 V for anode half-cell. Electrochemical testing was carried out with a BCS-805 Biologic battery cyclers (Biologic, France). The cells were discharged and charged at a constant current corresponding to a C-rate of C/10, C/3 and 1C.

2.2.3 Scanning electron microscopy

The electrode sample was A small disc with a diameter of 2 mm was laser micro-machined from the as-dried electrode sample and clamped vertically using a small metal clip. The clip was fully immersed in a 15:2 ratio of epoxy resin to epoxy hardener (EpoFix, Struers) inside a plastic mould of 20 mm diameter. The mould, containing the resin, clip and sample, was placed in a desiccator and degassed under dynamic vacuum for 1 h before being left in the desiccator overnight under static vacuum to ensure minimal gas remained in the sample. The as-cured

puck was subsequently hand-ground using a set of incrementally finer SiC papers (CarbiMet, Buehler), starting at P320 coarseness and finishing at P4000 coarseness, with interim IPA cleaning in a sonicator and visual inspection with an optical microscope (VHX-7000, Keyence) to ensure the previous grinding grooves had disappeared. To minimise charging in the scanning electron microscope (EVO 10, Carl Zeiss), the smoothed epoxy-puck was Au-coated (SC7620, Quorum) for 60 s at 18 mA, giving a Au-coating thickness of the order of tens of nanometres.

3 Results and discussion

3.1 Reference tests for acoustic measurements

Figure 1 (a) demonstrates the principles of pulse-echo ultrasound acoustic measurements to analyse electrode coatings. In this mode the ultrasound wave is emitted by a transducer and reflected at each interface with the reflected wave subsequently recorded by the same transducer. The reflected paths of ultrasonic waves though electrode-coating layers and the interfaces are shown in Figure 1 (b)-(d), respectively. As the ultrasound wave is a mechanical wave which requires a conductive medium to propagate, the path it takes in a dried electrode can only be facilitated through AM particles in direct contact, consequently there are a large number of reflections which occur at the edge of exposed electrode particles (i.e. solid-air interfaces). This has the effect of attenuating the energy of the ultrasonic wave as it passes through the dry electrode. However, during the early stages of the drying process, the solvent acts as a propagation medium for ultrasonic waves. By monitoring this dynamic change as the solvent is removed from the electrode it is possible to study the LIB electrode DP. There are several interfaces formed in LIB DP, as shown in Figure 1 (d), including the interface of the transducer and ultrasonic gel (solid-gel interface); the interface of the ultrasonic gel and CC (solid-gel interface, for which the ultrasonic gel is stable during the DP); the interface of CC and solvent (solid-liquid interface) at the beginning stage of drying; the interface of CC and solid AM particles (solid-solid interface) at the end of DP; and air-solid interface after drying finish.

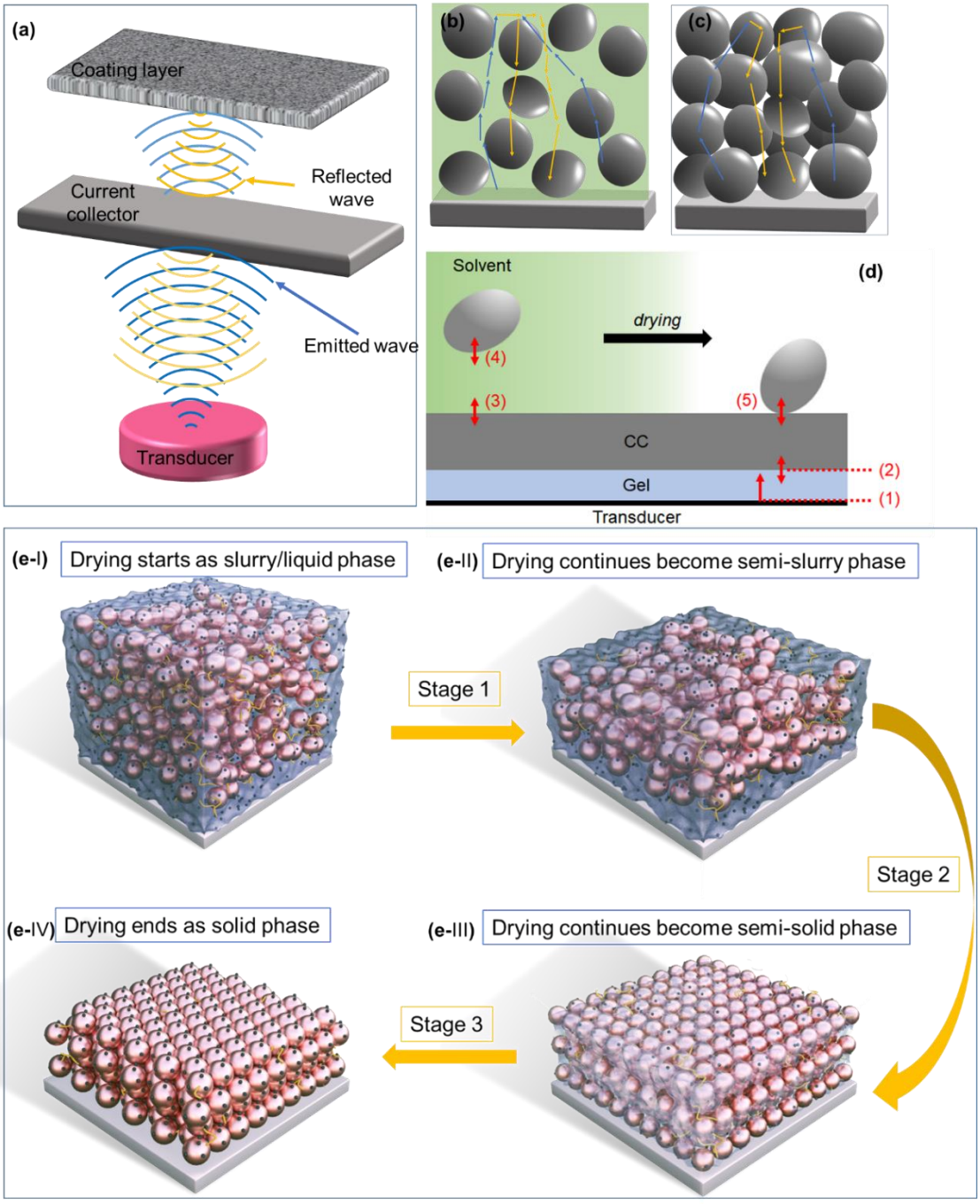

Figure 1 (a) Schematic diagram of ultrasonic reflection of electrode; (b) schematic diagram of reflected paths of ultrasonic waves through a wet slurry electrode coating with solvent (green colour indicates the solvent, grey shapes indicate active material particles, grey substrate indicates the current collector, blue arrows indicate the outbound ultrasound wave and yellow arrows indicate the reflective ultrasound waves). The ultrasonic waves transfer through both solvent and particles; (c) schematic diagram of the reflected paths of ultrasonic waves through dried solid electrode (without solvent). The ultrasonic waves transfer only through particles; (d) schematic diagram of interfaces in electrode drying process, which ToF shifts occur as interfaces (3) - (4) diminishes and transits to interface (5); (e) three-stage drying mechanism. Stage 1 is from slurry phase (e-I) to form a semi-slurry (e-II), stage 2 is following with the further removal of solvent (e-III) and stage 2 ends up with a compacted solid film of coating (e-IV) (yellow lines indicate the binder, pink particles indicate active material particles, black dots indicate the conductive carbon and light blue colour indicates the solvent).

To gain a full understanding of the acoustic ToF results, it is necessary to understand the internal structures of the electrode. To this end, scanning electron microscopy was performed to provide a description of the architecture of the electrode after drying, as shown in Figure 2 (c), where the condensed top film is the CC and adherent electrode coating film consists of dispersed AM particles. As a reference, the acoustic signals reflected by bare Al and Cu CC foils, as shown in Figure 3 (a) and 3 (b) respectively, are recorded along with the signals of the CCs with their corresponding cathode and anode slurry coatings (Figure 3 (d) and 3 (e)). The ToF response of the Al foil contains clear periodic peaks between 1 – 2 µs (Figure 2 (a)), whereas the amplitude and periodicity became irregular when the Al foil was coated with the cathode slurry as shown in Figure 2 (d), indicating multiple reflective paths taken by the ultrasound waves. Similarly, Figure 2 (b) is the acoustic signal received from the reflection of Cu foil which appeared simple and sharp compared to the anode as shown in Figure 2 (e).

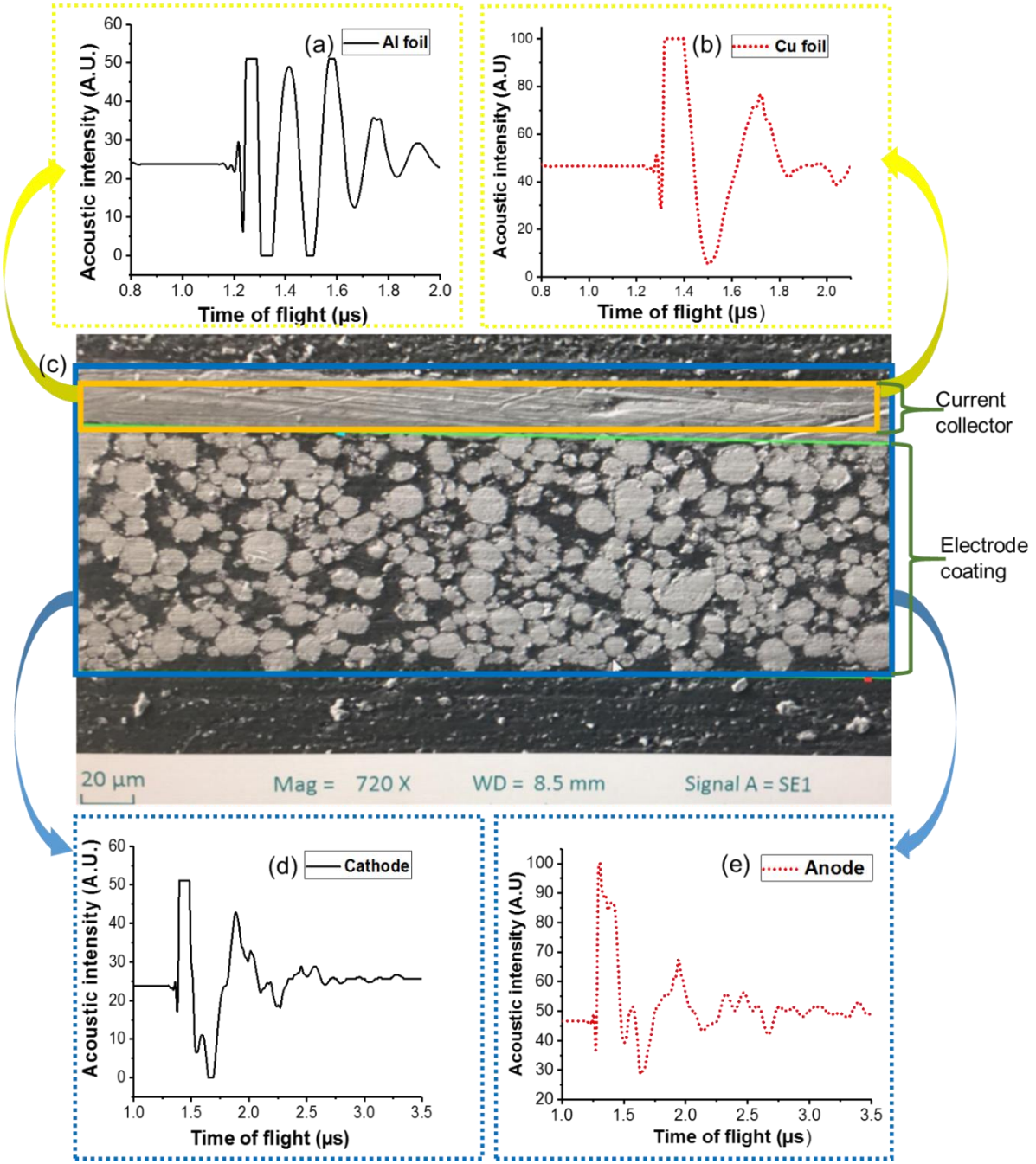

Figure 2 Acoustic signals for (a) bare Al foil, (b) bare Cu foil, (c) architecture of electrode cross-section scanned by scanning electron microscope (Zeiss EVO 10); (d) cathode slurry coating and (e) anode slurry coating.

3.2 *In-situ* acoustic measurements during the drying process

To better compare the signal evolution over the period of drying, the discussion focusses only on the first reflection peaks which indicating the CC-solvent interface at the early stage of drying and CC-solid particle interface at the end of dying. Figure 3 (a) shows the 2D ToF map of cathode drying at 60 °C, Figure 4 (a) shows the ToF map for the cathode dried at 40 °C and Figure 5 (a) shows that of the anode dried at 60 °C. The amplitudes of the reflected ultrasound

signals were mapped on a colour-scale ranging from lighter to darker shades as shown in the coloured scale bars. The cathode colour maps are presented in the blue colour spectrum and anode is in yellow-pink colour spectrum. Figure 3 (b) shows the attenuation of the ultrasonic wave during cathode drying at 60 °C, Figure 4 (b) is for the cathode dried at 40 °C, and Figure 5 (b) is for the anode dried at 60 °C, which the arrow colour scale bar indicates the increasing of the drying time.

Figure 3 (b) clearly shows two split peaks at ToF between 0.02-0.25 µs between 0 and 6 min of the drying stage which could be attributed to the slurry phase of the cathode coating at the beginning stage of drying (0-6 min), with the presence of a dominant solid-liquid interface of the CC and the solvent. This is evident for the cathode dried at 40 °C, as shown in Figure 4 (b), and also for the anode dried at 60 °C, as shown in Figure 5 (b), with a CC-anode slurry interface. However, the merging of peaks at ToF between 0.02-0.25 µs for the cathode dried at 40 °C is not significant until 12 min which is probably due to the slower rate of solvent removal. The merging of the peaks at ToF between 0.02-0.25 µs for the anode dried at 60 °C in Figure 5 (b) seems to be completed within 6 min, comparable with the cathode dried at 60 °C shown in Figure 3 (b). This could be due to the type of solvent for making anode slurry is water and NMP for making cathode slurry, that NMP has lower vapour pressure compared to water, therefore, slower rate of evaporation. At 60 °C, NMP's vapour pressure is ~ 0.4 kPa and water is ~19.93 kPa [47]. The merged peaks could correspond to the consolidation of the cathode coating film from the initial slurry phase.

The phase change of this drying stage has been extensively studied [21, 48-49], the schematic the most up-to-date electrode three-stage drying mechanism is shown in Figure 1(e) It can be explained as the initial stage of drying (Figure 1 (e-I) to (e-II)), where the solvent evaporates at a constant rate from the film surface. As the solvent at the surface evaporates, more solvent is transported upwards toward the surface. This stage of drying has also been elucidated which is characterised by solvent continuing to evaporate from the film surface at a constant rate as the solvent is transported towards the surface *via* capillary action. Most of pore emptying is governed by solvent evaporation at the surface of the coating, creating a surface tension gradient (Marangoni flow). This liquid flow is expressed by Darcy's law (permeability multiplied by the gradient of capillary pressure) [50]. The removal of solvent from between the AM particles causes them to get closer together and the film thickness decreases due to the outflow of liquid from the pores. The pressure gradient causes efficient suction from the pores due to capillary pressure, as described by Young-Laplace equation [23].

The ultrasonic response signals showed no significant evolution after 6 min in terms of shifting or attenuation for both cathode and anode drying at 60 °C, as shown in Figure 3 (b) and Figure

5 (b), respectively. This could correlate to the stable phase of the cathode coating where no further physical changes to the coating occurs, in terms of density and thickness. This initial drying stage 1 ends when the pore volume begins to empty as shown in Figure 1 (e-III). The onset of pore emptying can be observed from a change in the film surface [22]. This change usually coincides with the end of film shrinkage, i.e. the point where the AM particles form a compact structure, and the film thickness cannot decrease any further. The constant drying rate extends beyond the onset of pore emptying. This continuation indicates that there is efficient internal mass transfer through the compact pore structure due to capillary forces [50]. Large pores tend to empty preferentially according to the Young-Laplace equation, while small pores remain filled with solvent for longer [23, 51,52]. The onset of pore emptying has been identified as the first characteristic drying time, associated with the start of an intermediate drying stage that is sensitive to high drying rates [21]. This sensitivity can result in the detrimental loss of adhesion strength due to a depletion of binder in the vicinity of the coating/substrate interface under high drying rates. It could also explain the delayed peak-merging for the cathode dried at 40 °C, because the lower temperature induces a slower drying rate. A slower drying rate would promote an even distribution of binder The hypothesis to explain binder migration/inactive material segregation is that the capillary transport of the solvent draws additives along with it towards the surface. Binder accumulation at the evaporation surface has also been linked to the proliferation of cracks during drying [18].

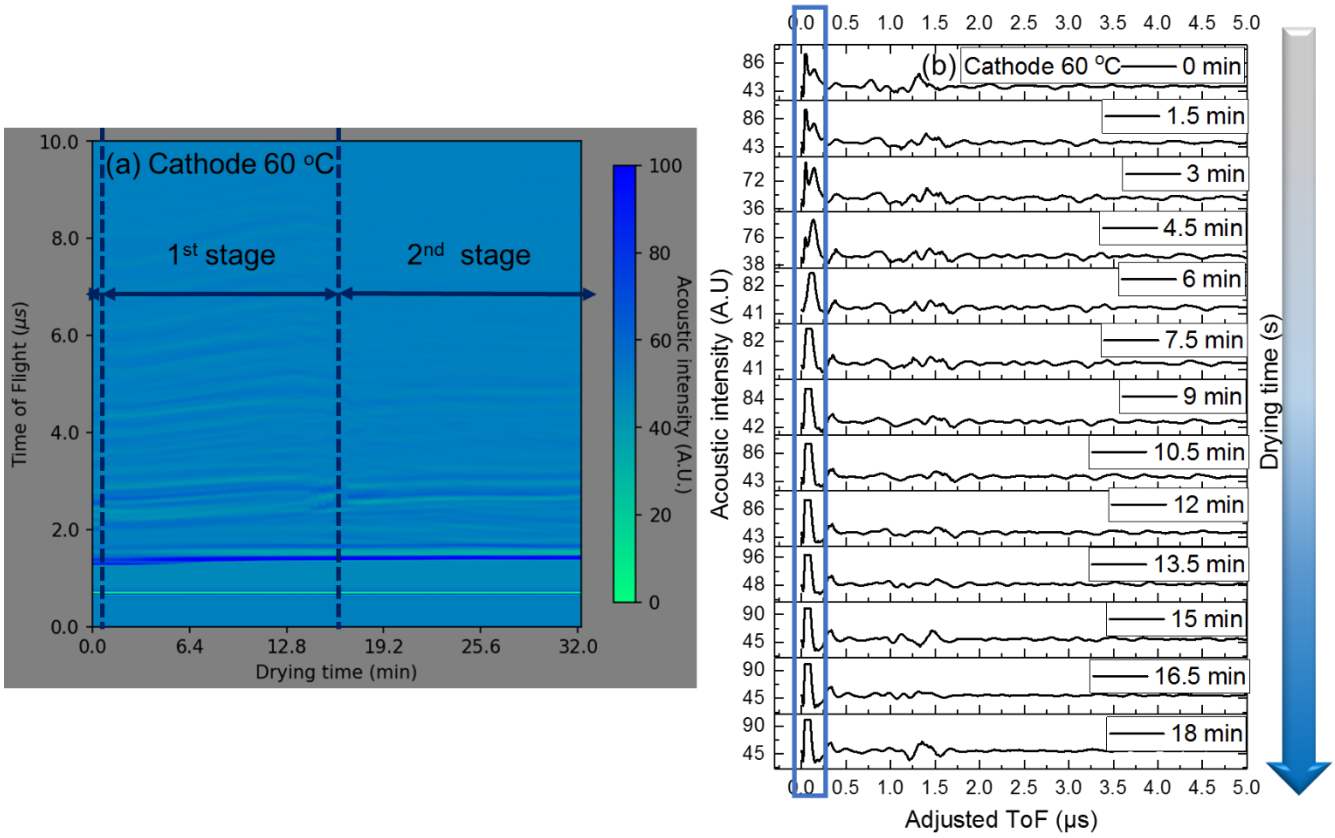

Figure 3 (a) Colour map of acoustic intensities and ToF during cathode coating layer drying at 60 °C (The scales of X- and Y-axis are adjusted to better illustrate the results, which the unit for X-axis is larger than the unit of Y-axis); (b) acoustic response evolution during drying process (the adjusted ToF are aligned after similarity analysis, and the details will be described in later session).

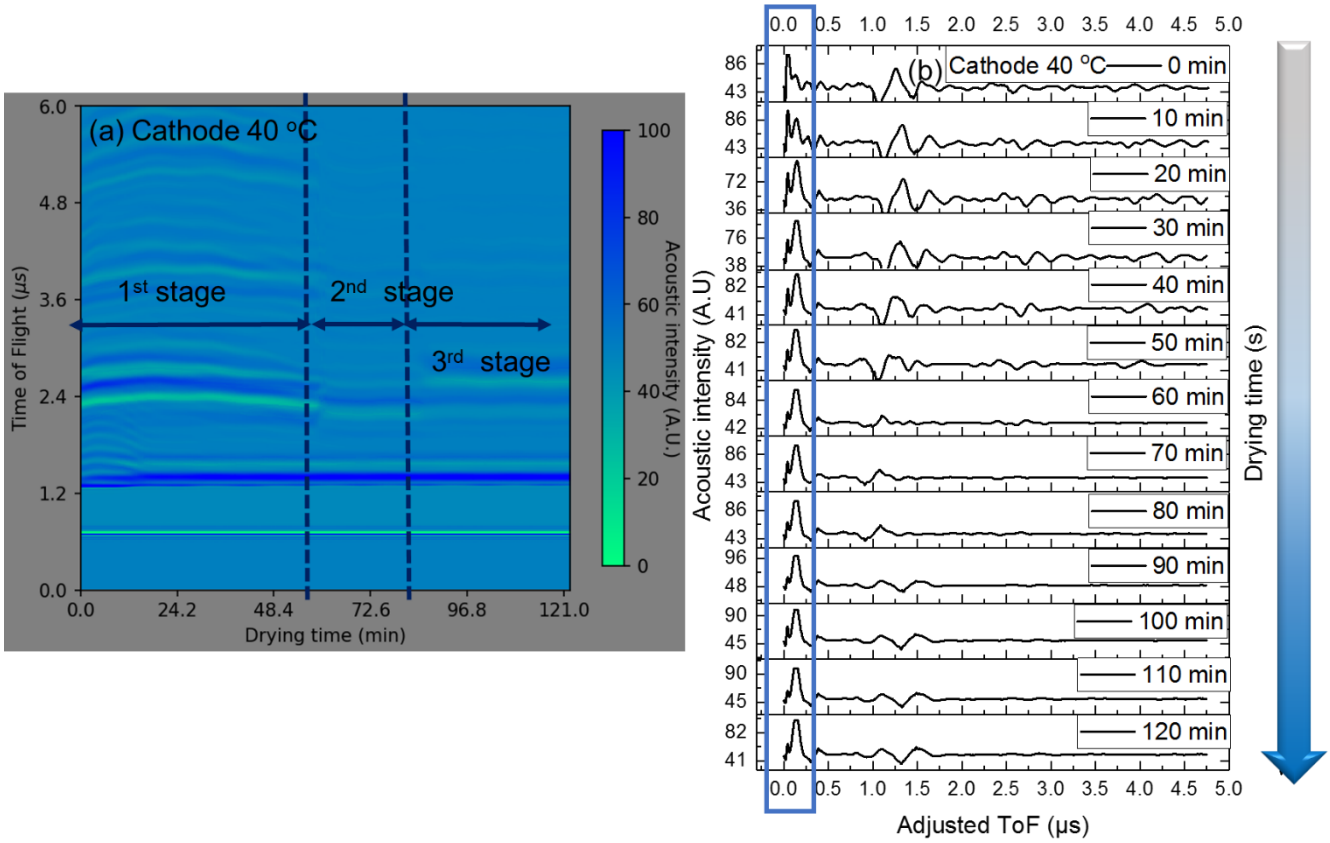

Figure 4 (a) Colour map of acoustic intensities and ToF during cathode coating layer drying at 40 °C (The scales of X- and Y-axis are adjusted to better illustrate the results, which the unit for X-axis is larger than the unit of Y-axis); (b) acoustic response evolution during the drying process (the adjusted ToF are aligned after similarity analysis, and the details will be described in later session).

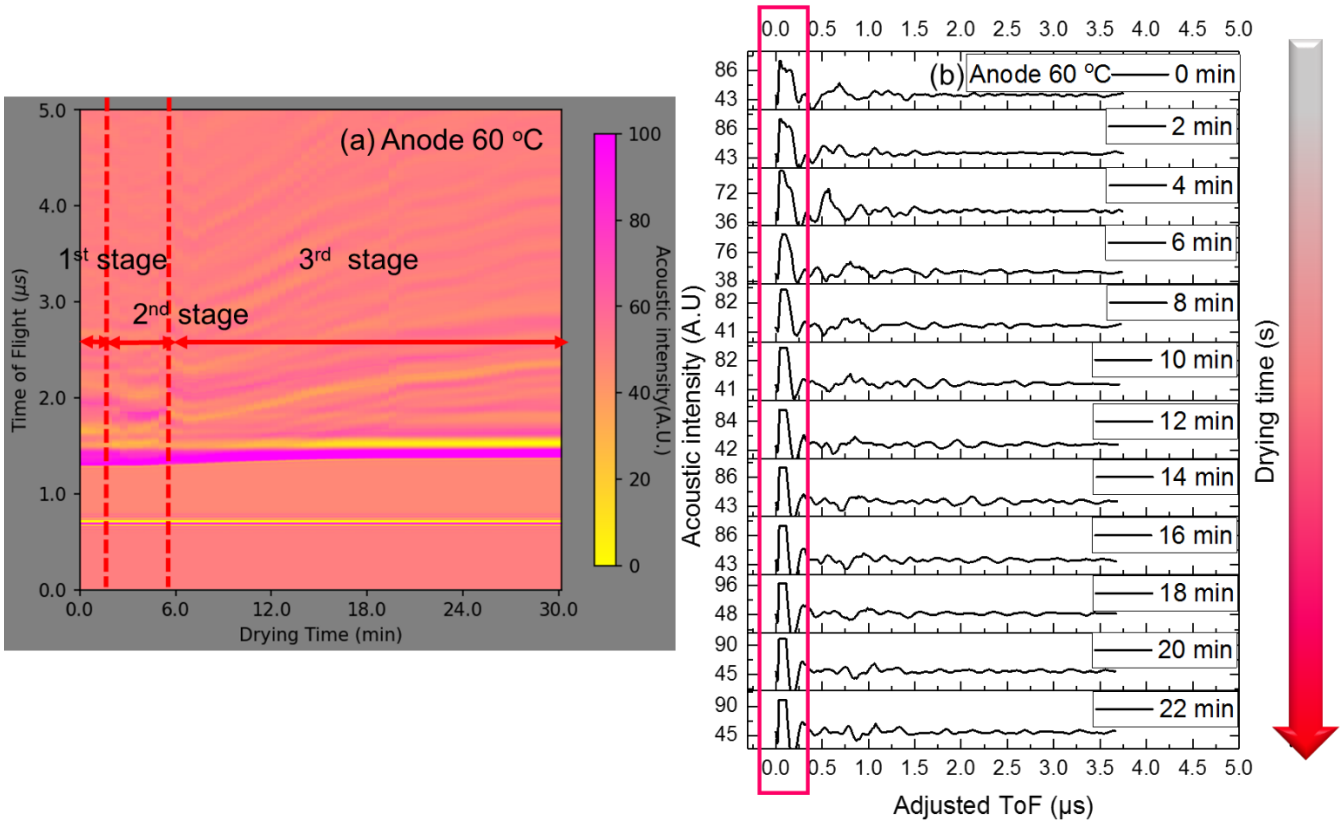

Figure 5 (a) Colour map of acoustic intensities and ToF during anode coating layer drying at 60 °C (The scales of X- and Y-axis are adjusted to better illustrate the results, which the unit for X-axis is larger than the unit of Y-axis); (b) acoustic response evolution during the drying process (the adjusted ToF are aligned after similarity analysis, and the details will be described in later session).

3.3 Similarity analysis of time-of-flight signals

The acoustic ultrasound signal is sensitive to physical property change of the materials especially at high temperature, and the research is focused on the coating itself. Therefore, the signal change that occurred before the interface of the ultrasound gel and CC is disregarded. Figure 6 (a), (c) and (d) show the progressive movement of the reflected peaks at the interface of the ultrasound gel and CC (solid-gel interface) during the DP. Although the phase of the ultrasonic gel remained unchanged during the DP, the elevated temperature could have affected the viscosity of the gel, thereby progressively shifting the position of the first reflected peak as shown in Figure S2. As the physical property of the gel is not involved in the LIB electrode DP, the positional shift induced by its varying viscosity was corrected by identifying the positions of the first reflected peak (as shown in Figure 6(a), (c) and (e)) and aligning it to ToF = 0 μs, as shown in Figure 3(b), Figure 4(b) and Figure 5(b).To prove the alignment of the ultrasound waves will not change the original shape of the signals, the similarity analyses of the ultrasound waves for each experiment before and after alignment

have been done. The ultrasound waves have been aligned similarly for all experiments, as shown in Figure 7 (a), (d) and (g).

Similarity analysis for the series of ultrasound waves for each experiment was then performed on the ToF signals without alignment, as shown in Figure 6 (b) for the cathode dried at 60 °C, Figure 6 (d) for the cathode dried at 40 °C, and Figure 6 (f) for the anode dried at 60 °C. The similarity index was obtained by performing cross-correlation of each ToF signal over the period of drying with that of time = 0 s. When the ToF signal is identical to the initial signal (drying time = 0 s), the similarity value is +1, whereas if the ToF signal has shifted such that it doesn't appear identical to the initial ToF signal, the similarity value is ~0. The similarity value becomes -1 when the ToF signal appears inverted compared to the initial ToF signal. The similarity index, therefore, provides a global average shift of the ultrasound waves as drying progresses. In general, the results indicate that the similarity of the ultrasonic wave decreases as the drying time increases.

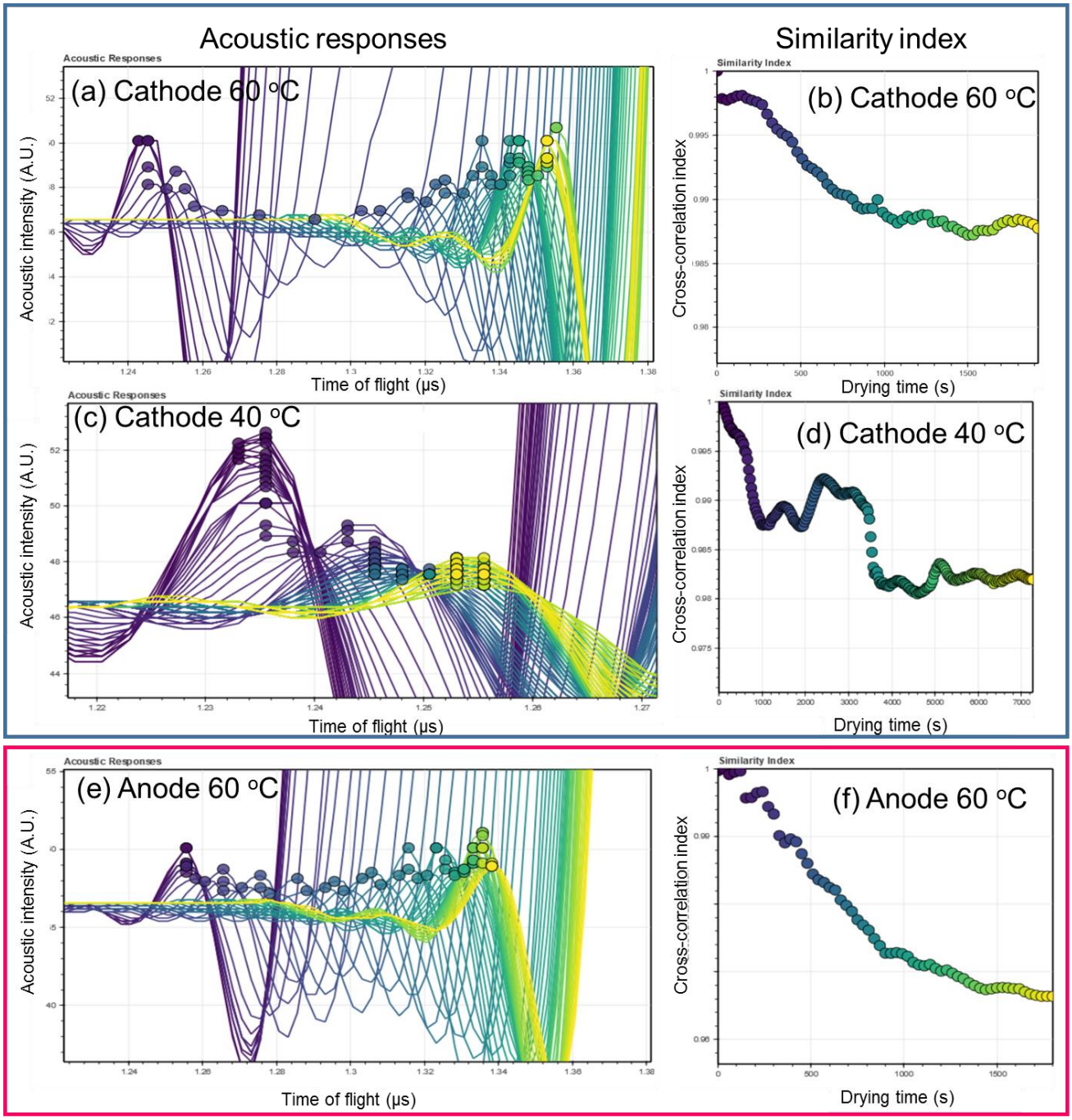

Figure 6 Similarity analysis of ToF signals without alignment for cathodes dried at 60 (a)-(b) and 40 °C (c)-(d), and anode dried at 60 °C (e)-(f) (the dots in (a), (c) and (e) indicate the identified first peaks; the different colours indicate the similarity of the ultrasound wave).

The similarity analysis was also performed on the entire ToF signal after aligning the peaks at ToF = 0 s for cathodes dried at 60 and 40 °C, and anode dried at 60 °C as shown in Figure 7. For all acoustic measurement experiments (cathode dried at 40 and 60 °C and anode dried at 60 °C), the decreasing similarities after alignment as shown in Figure 7 (b), (e) and (h) were similar to the decreasing similarities before alignment shown in Figure 6 (b), (d) and (f). This strengthens our assumption that the physical change of the ultrasonic gel does not influence the ToF evolution of the electrode, and the alignment benefits the interpretation about the

signal evolution during the DP. All the results show a decrease in the similarity, especially for the cathode and anode dried at 60 °C which show a linear decrease. These highlight a directional movement of the acoustic peaks that is a strong indication of drying. Therefore, the trends in similarity figures shown in Figure 7 (b), (e) and (h) represent the overall drying profiles of the slurry. Further, comparison of the ToF signals over the drying period will be discussed in the next section.

Upon alignment of the ToF signals, the peaks representing the CC were identified and tracked over the drying period, using a peak-tracing algorithm written on Python. The peak-trace profiles (Figure 7 (c) and (i)) show that two peaks merge together with the exception of the cathode and anode dried at 60 °C. Figure 7 (f) shows that the overlapping peaks at ToF range of 0.025-0.25 µs for cathode dried at 40 °C does not merge completely, in agreement with Figure 4 (b), which can be attributed to the slower drying rate at the lower temperature. This further supports sensitivity of the onset of pore emptying to high drying rates [21].

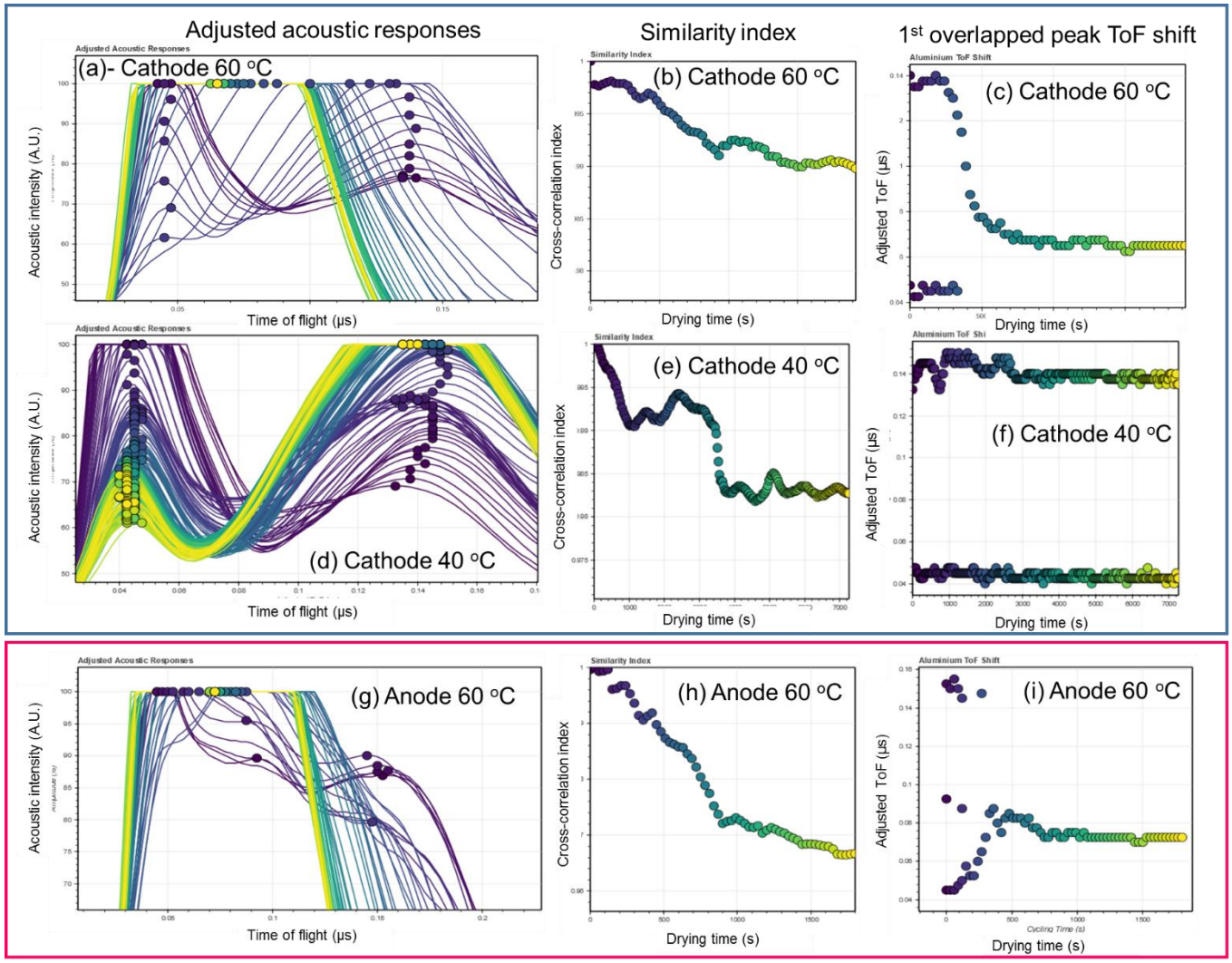

Figure 7 The adjusted ToF responses with alignment after similarity analysis for cathodes dried at 60 °C (a), 40 °C (d), and anode dried at 60 °C (g). Similarity analysis of ToF signals after alignment for cathode dried at 60 °C (b), cathode dried at 40 °C (e), and is for the anode dried at 60 °C (h). Adjusted ToF for the 1st overlapping peaks for cathodes dried at 60 (c) and 40 °C (f), and anode at 40 °C (i).

3.4 Time-of-flight evolution during the electrode drying process

After the alignment of the ultrasound signal for all experiment, the ToF evolution during LIB electrode DP is discussed in this section. As shown in Figure 8 (b), Figure 9 (b) and Figure 10 (b), the left half of the overlapping peaks (at ToF between 0.025-0.25 µs) indicates the interface of gel and CC (solid-slurry interface), and right half of the overlapping peak indicates the CC-solvent interface (solid-liquid interface at the beginning of drying and solid-solid interface at the end of drying).

The Figure 8 (a) illustrates the entire acoustic ToF evolution of the cathode coating layer dried at 60 °C, which shows the first peak increasing in amplitude until becoming saturated as it merges with the neighbouring peak. Figure 8 (b) shows the acoustic ToF evolution in the 1st stage of drying corresponding to the colour map in Figure 3 (a) between 1-16 min. As shown in Figure 8 (b), as the drying time increases, the left of the first overlapping peak attenuates and the right of the overlapping peak grows up. These shifts of ultrasonic waves resulted by the constant solvent evaporation result to volume reduction and film shrinkage as the initial stage of conventional drying mechanism [26, 33 33], as shown in Figure 1 (e-I) - (e-II). These shifts can also be explained as the attenuation of the reflective ultrasonic signal of solid-slurry will be greater since reflection and scattering at the solid-slurry interface is much stronger than the solid-liquid interface. Alternatively, the increasing amplitude of the right half of the peak as the drying time increases until the electrode is dried at end of the DP ~360 s is due to the attenuation of the ultrasonic signal at the solid-solid interface that is much smaller than at the solid-liquid interface. Similar results were also observed for the cathode dried at 40 °C, as shown in Figure 9 (b) and the anode dried at 60 °C in Figure 10 (d).

Figure 8 (b) also shows the right half of the overlapping peak shifting to left until merging with the right half of the peak for the cathode drying at 60 °C during drying, which could be the reflection and scattering of the ultrasonic wave at the interfaces in the different stages of drying. As the drying time increases, the cathode coating becomes denser until becoming a solid phase, consequently resulting in a faster response of the ultrasonic signal reflection due to higher material stiffness/elastic moduli. The top-down film consolidation mechanism was summarized by Jaiser *et al.* [15]. The consolidation layer of the electrode is rapidly formed on the surface of the electrode, even at low stiffness/elastic moduli of slurry, with no sedimentation. The consolidation layer grows as the solvent evaporates and the consolidation layer area expands until it approaches the substrate.

Figure 8 (c) shows the acoustic ToF evolution in the 2nd stage of drying corresponding to the colour map in Figure 3 (a) after 16 min, which has no significant change of the ultrasonic waves. However, the zoomed figure, as shown in Figure 8 (d), indicates a slight shift of the

ultrasonic wave to the right (longer ToF). This phenomena could be due to the further expansion of the solid cathode coating that subsequently prolong the measurement of the reflection of the ultrasonic wave from the CC/cathode coating interface. The further shift of the ultrasonic wave does not occur for the cathode dried at 40 °C, as shown in Figure 9 (c) and (d). This is also means the delayed reflection of ultrasonic wave could be due to the lower temperature not inducing thermal expansion of the cathodes after formation of the consolidated film.

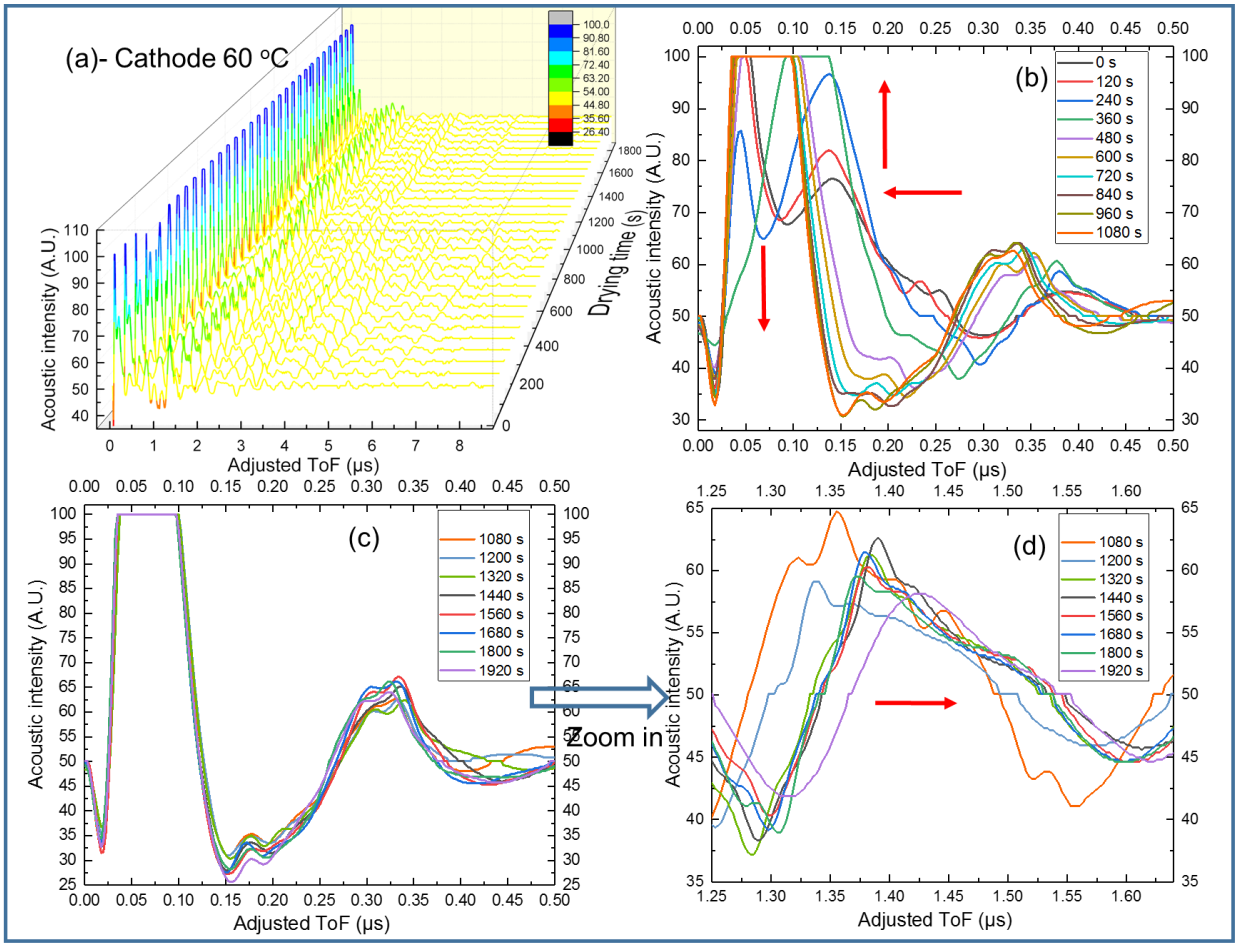

Figure 8 (a) Acoustic ToF evolution during cathode coating layer dried at 60 °C; (b) acoustic ToF evolution during the 1st stage of drying; (c) acoustic ToF evolution during the 2nd stage of drying; (d) zoom-in acoustic ToF evolution during the 2nd stage of drying.

The Figure 9 (a) illustrates the entire acoustic ToF evolution for the cathode coating layer dried at 40 °C, showing that the first half of the overlapping peak at ToF between 0.025-0.25 µs increases in amplitude until saturated. Figure 9 (b) shows the acoustic ToF evolution during the 1st stage of drying, corresponding to the colour map in Figure 4 (a) between 1-50 min. Apart from the similar peak evolution discussed earlier, that the left half of the overlapping

peak decreases and the right half of the peak increases. The overlapping peak does not shift to the left compared to that of the cathode dried at 60 °C. This could be due to the slow drying rate at the relatively low temperature that would keep the slurry phase of coating for a longer period without interfering the reflection of ultrasonic wave signals form the interface of CC and cathode coating. Correspondingly, the attenuation of the ultrasonic wave will be less significant but take longer time to attenuate compared with the cathode dried at higher temperature.

Figure 10 (c) shows the acoustic ToF evolution during the 2nd stage of drying corresponding to the colour map in Figure 5 (a) between 50-85 min. Figure 10 (d) shows the acoustic ToF evolution during the 3rd stage of drying, corresponding to the colour map in Figure 5 (a) after 85 min. The ultrasonic response slightly shift vertically without any trends after 3000 s, this could be explained as the large pores become depleted of solvent, only isolated patches of solvent remain within the capillary network. During this final stage, the solvent evaporates at the internal gas-liquid interfaces and must then diffuse as vapour out of the film. The additional mass transport resistance due to vapour diffusion through the pore structure reduces the drying rate [21].

Jaiser *et al.* [21] found that no further adhesion loss is caused by using a high drying rate to accelerate this final stage of drying. This insensitivity can be explained by the isolation of the inactive material in disconnected pores between which it is unable to move, preventing any further binder migration. This final stage ends when all solvent is removed, and the film is completed dry as shown in Figure 1 (e-IV).

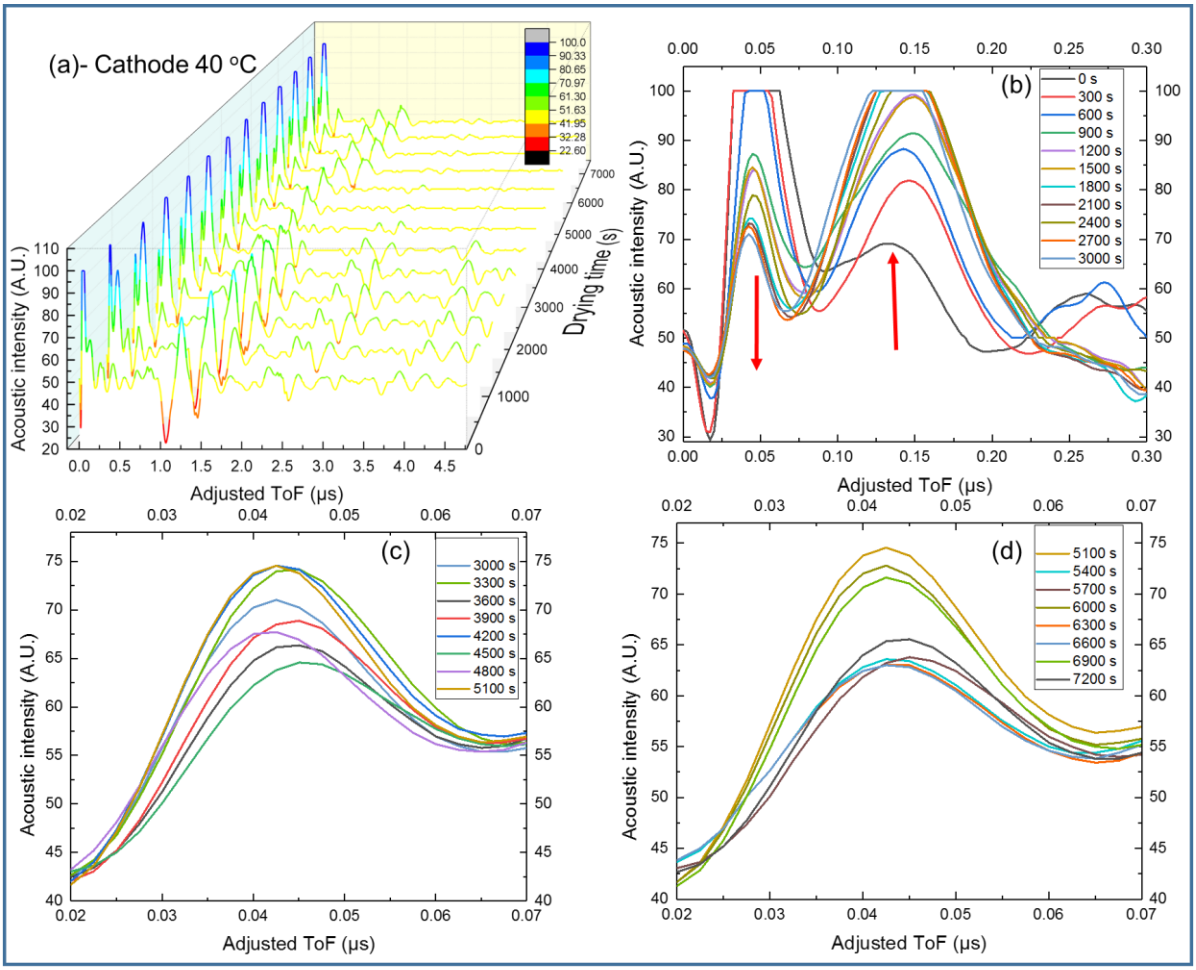

Figure 9 (a) Acoustic ToF evolution during cathode coating layer dried at 40 °C; (b) acoustic ToF evolution during the 1st stage of drying; (c) acoustic ToF evolution during the 2nd stage of drying; (d) acoustic ToF evolution during the 3rd stage of drying.

Figure 10 (a) illustrates the entire acoustic ToF evolution for the anode coating layer dried at 60 °C, showing that the left half of the overlapping peaks which at ToF between 0.025-0.25 µs increase in amplitude until saturated. Figure 10 (b) shows the acoustic ToF evolution during the 1st stage of drying corresponding to the colour map in Figure 5 (a) between 0-3 min. Figure 10 (c) shows the acoustic ToF evolution during the 2nd stage of drying corresponding to the colour map in Figure 5 (a) between 3-6 min. There are no significant changes of the ultrasonic response in the first two stages of drying within 6 min. This could be caused by the fact that the specific heat capacity of NMP (~1259J kg^{-1} $°C^{-1}$) is lower than the specific heat capacity of water (4200 J kg^{-1} $°C^{-1}$), thereby taking longer for anode slurry to heat-up.

Figure 10 (d) shows the acoustic ToF evolution during the 3rd stage of drying corresponding to the colour map in Figure 5 (a) after 6 min. The evolution of ultrasonic response demonstrates a similar trend as the cathode drying at 60 °C, as shown in Figure 10 (b) which

shifts to the left (shorter ToF). This can also be explained as the reflection and scattering of the ultrasonic wave at the interfaces in the different stages of drying that have different physical properties, including the density. As the solvent is being continuously removed during the DP, the density, stiffness/elastic moduli of the anode coating film increases that result in a faster response of the ultrasonic signal reflection. The first two peaks of the initial ultrasonic ToF signal (from drying time = 0 s) appear much closer together to begin with, when compared with the first two peaks of the cathodes, as shown in Figure 8 (b) and Figure 9 (b). This significant overlapping of the two peaks in the anode could be due to a similar attenuation of the ultrasound between the ultrasound gel-CC interface and the CC-anode slurry. It has been reported that the water-based anode slurry is predominantly elastic, while the organic-based cathode slurry is predominantly viscous, which indicates that the viscosity of the organic-based cathode slurry is better than the anode slurry for acoustic resolution [18]. As shown in Figure 10 (d), the ultrasonic wave attenuates as drying times increase, this is caused by the consolidation of the anode coating film resulting in greater attenuation of the ultrasonic signal at solid-solid interfaces than solid-liquid interfaces in the presence of solvent.

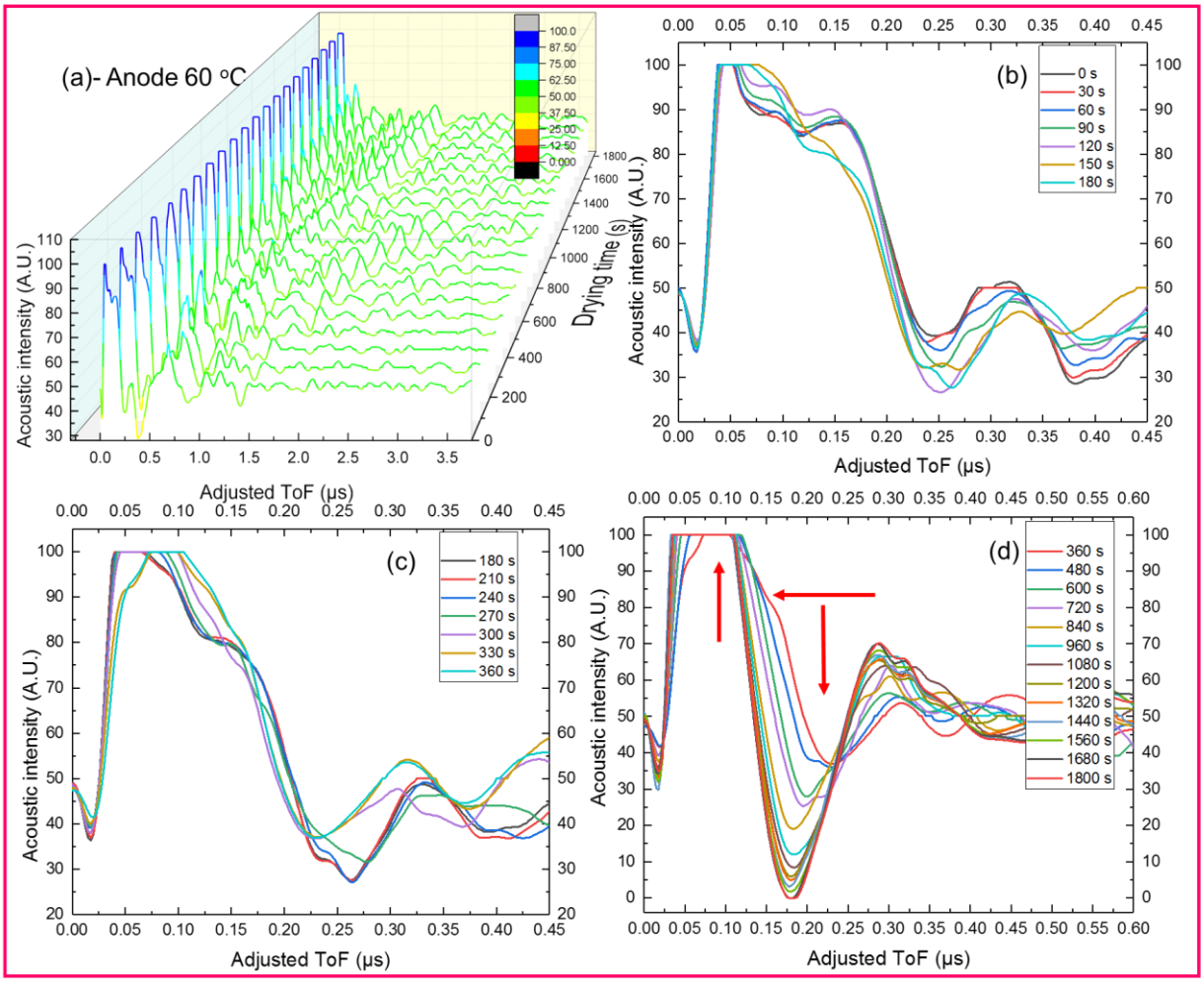

Figure 10 (a) Acoustic ToF evolution for the anode coating layer dried at 60 °C; (b) acoustic ToF evolution during the 1st stage of drying; (c) acoustic ToF evolution during the 2nd stage of drying; (d) acoustic ToF evolution during the 3rd stage of drying.

3.5 Electrochemical testing

Electrochemical properties of the cathodes dried at 40 and 60 °C, and anode dried at 60 °C were tested in coin cells with different C-rates C/10, C/3 and 1C. Figure 11 (a)-(b) shows the discharge and charge performances for cathodes dried at 60 °C, which shows that the specific capacity is highest at C/10 for both charged and discharged states. Figure 11 (c)-(d) shows the discharge and charge performances of the cathode dried 40 °C, the specific capacity is highest at C/10 during charge, but the highest discharge capacity is at C/3. As shown in Figure 11(e)-(f), discharge and charge performances for the anode dried at 60 °C are showing similar trends, which the slower C-rate has higher specific capacity. Figure 11 (g) illustrates the specific capacities for each electrode at different C-rates. At all C-rates, the cathode dried at 40 °C has higher specific capacity comparing with the cathode dried at 60 °C. This can be explained as the slow drying rate would promote a more homogenous CBD distribution, which could boost the electrode's performance. It has been reported that the drying rate is

determined by the drying temperature [12]. The optimized drying rate during the electrode manufacturing process will promote the balanced binder distribution of electrode film. However, the higher drying rate will result in an uneven distribution of soluble and dispersed binder throughout the electrode, potentially accumulating at the surface [15, 18-20]. This binder migration can also lead to electrode delamination [12-13, 20, 24], due to the reduction in adhesion strength at the CC-electrode interface. High temperatures have been reported to potentially lead to greater binder migration, which can cause electrode delamination and result to a high resistance [12-13, 20, 24].

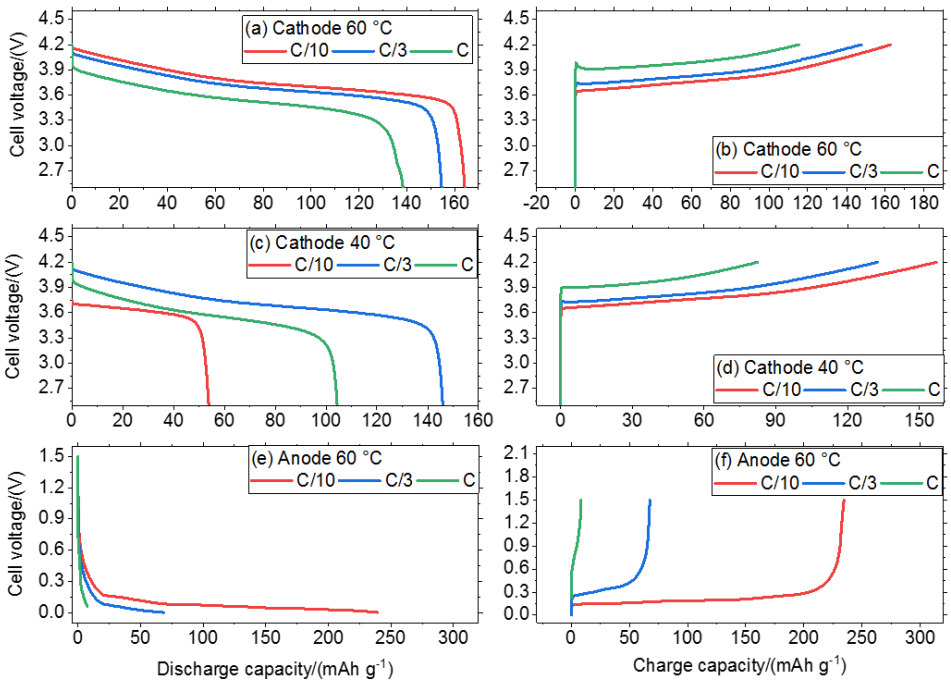

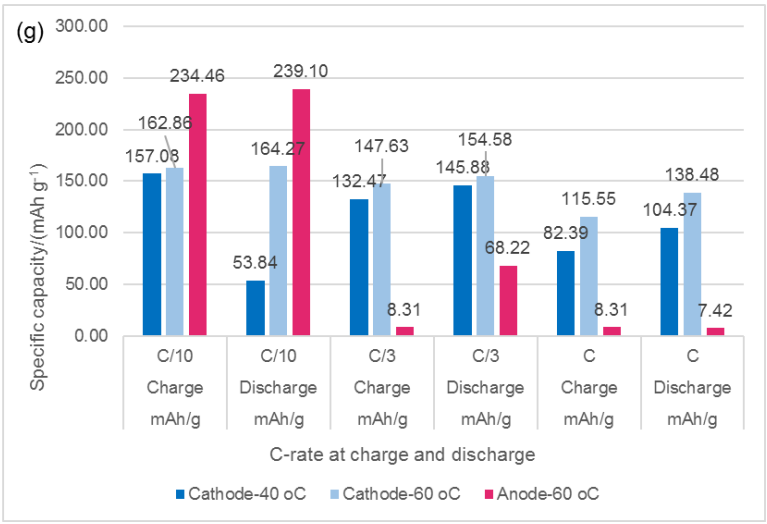

Figure 11 Comparison of discharge and charge performances for cathodes dried at 60 (a)-(b) and 40 °C (c)-(d), and anode dried at 60 °C (e)-(f) with C-rate at C/10, C/3 and 1C; (g) specific capacity check.

4 Conclusion

An ultrasound acoustic based technique has been applied as an *in-situ* metrology tool to study the LIB electrode drying process using an NMC622-based cathode and graphite-based anode. The dynamic evolutions of the cathode dried at 40 °C and 60 °C, and anode dried at 60 °C were investigated, and the attenuation and shifts of the reflected acoustic signals were discussed and correlated with the up-to-date three-stage drying mechanism. The vertical attenuation of the ultrasonic waves is due to the interfacial changes caused by solvent removal and evaporation governed by Darcy's law and the Marangoni effect. These shifts can also be explained as the attenuation of the ultrasonic signal at solid-slurry interface was greater since reflection and scattering at the solid-slurry interface is much stronger than at the solid-liquid interface. Conversely, the attenuation of the ultrasonic signal at the solid-solid interface was much smaller than the solid-liquid interface. The horizontal shifts of the acoustic signal was due to the reflection and scattering of the ultrasonic wave at the interfaces during the different stages of drying. As the drying time increases, the cathode coating became increasingly dense until it became one solid phase, resulting in a faster response of the ultrasonic signal reflection.

Ultrasound acoustic-based measurements have been successfully proven to be a powerful *in-situ* metrology to acquire dynamic drying profiles of LIB electrode during DP, which shows the potential of this rapid technique to be further developed for better understanding of DP to achieve a more controllable manufacturing process. The resulting electrochemical properties of the electrodes were tested in coin cells, where the cathode dried at lower temperature (40 °C) yielded higher specific capacities at all tested C-rates (C/10, C/3 and 1C) compared to the cathode dried at 60 °C. This was due to that the lower drying temperature would have promoted a more homogenous distribution of CBD, therefore promoting a better electrochemical performance.

In general, the TGA technique is a powerful tool to study the weight change during the drying of the slurry itself. Furthermore, the electrode drying process not only has weight change, but also has physical property evolution and the interfaces change of the slurry which acoustic measurement is powerful to provide these details. Also, acoustic measurement has the great potential to be applied in the electrode manufacturing process as an in-line tool, but TGA cannot.

References:

(1) Research, G. V. *Lithium-ion Battery Market Size, Share & Trends Analysis Report By Product (LCO, LFP, NCA, LMO, LTO, Lithium Nickel Manganese Cobalt), By Application, By Region, And Segment Forecasts, 2020 - 2027*; 2020.
(2) Kim, H.; Yoon, J.; Yoon, W.-S. In *Polymorphic Consideration in Conversion Reaction-Based Anode Materials for Next-Generation Li Rechargeable Batteries*, ECS Meeting Abstracts, IOP Publishing: 2020; p 544.
(3) Kendrick, E. Advancements in Manufacturing,*Future Lithium-ion Batteries*; Royal Society of Chemistry: 2019; pp 262-289.
(4) Danner, T.; Hein, S.; Westhoff, D.; Prifling, B.; Schmidt, V.; Latz, A. The Importance of Passive Materials in Li-ion Battery Electrodes. **2019**.
(5) Hawley, W. B.; Li, J. Electrode manufacturing for lithium-ion batteries-Analysis of Current and Next generation Processing. *Journal of Energy Storage* **2019,** *25*, 100862.
(6) Nowak, S.; Winter, M. Elemental Analysis of Lithium-ion Batteries. *Journal of Analytical Atomic Spectrometry* **2017,** *32* (10), 1833-1847.
(7) Bieker, P.; Winter, M. Lithium‐Ionen‐Technologie Und Was Danach Kommen Könnte: Hochenergieakkumulatoren. Teil 2 von 2. *Chemie in unserer Zeit* **2016,** *50* (3), 172-186.
(8) Froboese, L.; Titscher, P.; Westphal, B.; Haselrieder, W.; Kwade, A. Mercury Intrusion or Ion-and Conversion-Based Battery Electrodes–Structure and Diffusion Coefficient Determination. *Materials Characterization* **2017,** *133*, 102-111.
(9) Kwade, A.; Haselrieder, W.; Leithoff, R.; Modlinger, A.; Dietrich, F.; Droeder, K. Current Status and Challenges for Automotive Battery Production Technologies. *Nature Energy* **2018,** *3* (4), 290-300.
(10) Vetter, J.; Novák, P.; Wagner, M. R.; Veit, C.; Möller, K.-C.; Besenhard, J.; Winter, M.; Wohlfahrt-Mehrens, M.; Vogler, C.; Hammouche, A. Ageing Mechanisms in Lithium-ion Batteries. *Journal of Power Sources* **2005,** *147* (1-2), 269-281.
(11) Xu, M.; Reichman, B.; Wang, X. Modeling The Effect Of Electrode Thickness on the Performance Of Lithium-ion Batteries With Experimental Validation. *Energy* **2019,** *186*, 115864.
(12) Baunach, M.; Jaiser, S.; Schmelzle, S.; Nirschl, H.; Scharfer, P.; Schabel, W. Delamination Behavior of Lithium-ion Battery Anodes: Influence of Drying Temperature During Electrode Processing. *Drying Technology* **2016,** *34* (4), 462-473.
(13) Westphal, B.; Bockholt, H.; Günther, T.; Haselrieder, W.; Kwade, A. Influence of Convective Drying Parameters on Electrode Performance and Physical Electrode Properties. *ECS Transactions* **2015,** *64* (22), 57-68.
(14) Harris, D. J.; Lewis, J. A. Marangoni Effects on Evaporative Lithographic Patterning of Colloidal Films. *Langmuir* **2008,** *24* (8), 3681-3685, DOI: 10.1021/la8000637.
(15) Jaiser, S.; Müller, M.; Baunach, M.; Bauer, W.; Scharfer, P.; Schabel, W. Investigation of Film Solidification and Binder Migration During Drying of Li-Ion Battery Anodes. *Journal of Power Sources* **2016,** *318*, 210-219.
(16) Yuan, C.; Deng, Y.; Li, T.; Yang, F. Manufacturing Energy Analysis of Lithium ion Battery Pack for Electric Vehicles. *CIRP Annals* **2017,** *66* (1), 53-56.
(17) Postareff, L.; Lindblom-Ylänne, S. Emotions and Confidence Within Teaching in Higher Education. *Studies in Higher Education* **2011,** *36* (7), 799-813.
(18) Li, C.-C.; Wang, Y.-W. Binder Distributions In Water-Based and Organic-Based $Licoo_2$ Electrode Sheets and Their Effects on Cell Performance. *Journal of The Electrochemical Society* **2011,** *158* (12), A1361-A1370.

(19) Lim, S.; Ahn, K. H.; Yamamura, M. Latex Migration in Battery Slurries During Drying. *Langmuir* **2013,** *29* (26), 8233-8244.
(20) Hagiwara, H.; Suszynski, W. J.; Francis, L. F. A Raman Spectroscopic Method to Find Binder Distribution in Electrodes During Drying. *Journal of Coatings Technology and Research* **2014,** *11* (1), 11-17.
(21) Jaiser, S.; Friske, A.; Baunach, M.; Scharfer, P.; Schabel, W. Development of A Three-Stage Drying Profile Based on Characteristic Drying Stages for Lithium-ion Battery Anodes. *Drying Technology* **2017,** *35* (10), 1266-1275.
(22) Jaiser, S.; Funk, L.; Baunach, M.; Scharfer, P.; Schabel, W. Experimental Investigation Into Battery Electrode Surfaces: The Distribution of Liquid at The Surface and The Emptying of Pores During Drying. *Journal of Colloid and Interface Science* **2017,** *494*, 22-31.
(23) Jaiser, S.; Kumberg, J.; Klaver, J.; Urai, J. L.; Schabel, W.; Schmatz, J.; Scharfer, P. Microstructure Formation of Lithium-ion Battery Electrodes During Drying–An *Ex-Situ* Study Using Cryogenic Broad Ion Beam Slope-Cutting and Scanning Electron Microscopy (Cryo-BIB-SEM). *Journal of Power Sources* **2017,** *345*, 97-107.
(24) Müller, M.; Pfaffmann, L.; Jaiser, S.; Baunach, M.; Trouillet, V.; Scheiba, F.; Scharfer, P.; Schabel, W.; Bauer, W. Investigation of Binder Distribution in Graphite Anodes for Lithium-ion Batteries. *Journal of Power Sources* **2017,** *340*, 1-5.
(25) Pfaffmann, L.; Jaiser, S.; Müller, M.; Scharfer, P.; Schabel, W.; Bauer, W.; Scheiba, F.; Ehrenberg, H. New Method for Binder and Carbon Black Detection at Nanometer Scale in Carbon Electrodes for Lithium-ion Batteries. *Journal of Power Sources* **2017,** *363*, 460-469.
(26) Susarla, N.; Ahmed, S.; Dees, D. W. Modeling and Analysis of Solvent Removal During Li-ion Battery Electrode Drying. *Journal of Power Sources* **2018,** *378*, 660-670.
(27) Kaiser, J.; Wenzel, V.; Nirschl, H.; Bitsch, B.; Willenbacher, N.; Baunach, M.; Schmitt, M.; Jaiser, S.; Scharfer, P.; Schabel, W. Process and Product Development of Electrodes for Lithium‐Ion Cells. *Chemie Ingenieur Technik* **2014,** *86* (5), 695-706.
(28) Günther, T.; Billot, N.; Schuster, J.; Schnell, J.; Spingler, F. B.; Gasteiger, H. A. In *The Manufacturing of Electrodes: Key Process for the Future Success of Lithium-ion Batteries*, Advanced Materials Research, Trans Tech Publ: 2016; pp 304-311.
(29) Zheng, H.; Tan, L.; Liu, G.; Song, X.; Battaglia, V. S. Calendering Effects on the Physical and Electrochemical Properties of Li [Ni1/3Mn1/3Co1/3] O_2 Cathode. *Journal of Power Sources* **2012,** *208*, 52-57.
(30) Garsany, Y.; Singer, I. L.; Swider-Lyons, K. E. Impact of Film Drying Procedures on RDE Characterization of Pt/VC Electrocatalysts. *Journal of Electroanalytical Chemistry* **2011,** *662* (2), 396-406.
(31) Hwang, S.-W.; Hyun, S.-H. Synthesis and Characterization of Tin Oxide/Carbon Aerogel Composite Electrodes for Electrochemical Supercapacitors. *Journal of Power Sources* **2007,** *172* (1), 451-459.
(32) Liu, W.-w.; Yan, X.-b.; Lang, J.-w.; Peng, C.; Xue, Q.-j. Flexible and Conductive Nanocomposite Electrode Based on Graphene Sheets and Cotton Cloth for Supercapacitor. *Journal of Materials Chemistry* **2012,** *22* (33), 17245-17253.
(33) Stein, M.; Mistry, A.; Mukherjee, P. P. Mechanistic Understanding of the Role of Evaporation in Electrode Processing. *Journal of The Electrochemical Society* **2017,** *164* (7), A1616-A1627.
(34) Luo, H.; Cardinal, C. M.; Scriven, L. E.; Francis, L. F. Ceramic Nanoparticle/Monodisperse Latex Coatings. *Langmuir* **2008,** *24* (10), 5552-5561, DOI: 10.1021/la800050u.

(35) Ma, Y.; Davis, H. T.; Scriven, L. E. Microstructure Development in Drying Latex Coatings. *Prog. Org. Coat.* **2005,** *52* (1), 46-62.
(36) Buss, F.; Roberts, C. C.; Crawford, K. S.; Peters, K.; Francis, L. F. Effect of Soluble Polymer Binder on Particle Distribution in A Drying Particulate Coating. *Journal of Colloid and Interface Science* **2011,** *359* (1), 112-120.
(37) Kusano, T.; Hiroi, T.; Amemiya, K.; Ando, M.; Takahashi, T.; Shibayama, M. Structural Evolution of A Catalyst Ink for Fuel Cells During the Drying Process Investigated by CV-SANS. *Polymer Journal* **2015,** *47* (8), 546-555.
(38) Krebs, F. C. Polymer Solar Cell Modules Prepared Using Roll-To-Roll Methods: Knife-Over-Edge Coating, Slot-die Coating and Screen Printing. *Solar Energy Materials and Solar Cells* **2009,** *93* (4), 465-475.
(39) Higa, K.; Zhao, H.; Parkinson, D. Y.; Barnard, H.; Ling, M.; Liu, G.; Srinivasan, V. Electrode Slurry Particle Density Mapping Using X-ray Radiography. *Journal of the Electrochemical Society* **2017,** *164* (2), A380-A388.
(40) Lim, S.; Kim, S.; Ahn, K. H.; Lee, S. J. Stress Development of Li-ion Battery Anode Slurries During the Drying Process. *Industrial & Engineering Chemistry Research* **2015,** *54* (23), 6146-6155.
(41) Hsieh, A.; Bhadra, S.; Hertzberg, B.; Gjeltema, P.; Goy, A.; Fleischer, J. W.; Steingart, D. A. Electrochemical-Acoustic Time of Flight: In *Operando* Correlation of Physical Dynamics with Battery Charge and Health. *Energy & Environmental Science* **2015,** *8* (5), 1569-1577.
(42) Davies, G.; Knehr, K. W.; Van Tassell, B.; Hodson, T.; Biswas, S.; Hsieh, A. G.; Steingart, D. A. State of Charge and State of Health Estimation Using Electrochemical Acoustic Time of Flight Analysis. *Journal of The Electrochemical Society* **2017,** *164* (12), A2746-A2755.
(43) Robinson, J. B.; Maier, M.; Alster, G.; Compton, T.; Brett, D. J.; Shearing, P. R. Spatially Resolved Ultrasound Diagnostics of Li-ion Battery Electrodes. *Physical Chemistry Chemical Physics* **2019,** *21* (12), 6354-6361.
(44) Deng, Z.; Huang, Z.; Shen, Y.; Huang, Y.; Ding, H.; Luscombe, A.; Johnson, M.; Harlow, J. E.; Gauthier, R.; Dahn, J. R. Ultrasonic Scanning to Observe Wetting and "Unwetting" in Li-ion Pouch Cells. *Joule* **2020,** *4* (9), 2017-2029.
(45) Dance, D.; Christofides, S.; Maidment, A.; McLean, I.; Ng, K. Diagnostic Radiology Physics: A Handbook for Teachers and Students,, European Federation of Organisations for Medical Physics. *International Atomic Energy Agency (IAEA): IAEA* **2014**.
(46) Catapult, W. c. H., Battery Materials Scale-up & Cell Pilot Line Equipment List. Warwick Manufacturing Group, T. U. o. W., Ed. 2013; p 6.
(47) Kneisl, P.; Zondlo, J. W. Vapor Pressure, Liquid Density, and the Latent Heat of Vaporization as Functions of Temperature for Four Dipolar Aprotic Solvents. *Journal of Chemical and Engineering Data* **1987,** *32* (1), 11-13.
(48) Westphal, B. G.; Kwade, A. Critical Electrode Properties and Drying Conditions Causing Component Segregation in Graphitic Anodes for Lithium-ion Batteries. *Journal of Energy Storage* **2018,** *18*, 509-517.
(49) Font, F.; Protas, B.; Richardson, G.; Foster, J. M. Binder Migration During Drying of Lithium-ion Battery Electrodes: Modelling and Comparison to Experiment. *Journal of Power Sources* **2018,** *393*, 177-185.
(50) Tsotsas, Evangelos, and Arun S. Mujumdar, eds. Modern Drying Technology, Volume 2: Experimental Techniques. John Wiley & Sons, 2011.
(51) Metzger, T.; Tsotsas, E. Influence of Pore Size Distribution on Drying Kinetics: A Simple Capillary Model. *Drying Technology* **2005,** *23* (9-11), 1797-1809.

(52) Majasan J, Robinson J, Owen R, Maier M, Radhakrishnan AN, Pham M, Tranter TG, Zhang Y, Shearing P, Brett D. Recent Advances in Acoustic Diagnostics for Electrochemical Power Systems. *Journal of Physics: Energy* 2021, 3 032011.

Graphical abstract: